Journal of Computational Physics 229 (2010) 7488–7502

Contents lists available at ScienceDirect

Journal of Computational Physics

journal homepage: www.elsevier.com/locate/jcp

Fully implicit 1D radiation hydrodynamics: Validation and verification

Karabi Ghosh *, S.V.G. Menon

Theoretical Physics Division, Bhabha Atomic Research Centre, Mumbai 400 085, India

ARTICLE INFO

Article history:
Received 19 November 2009
Received in revised form 21 May 2010
Accepted 16 June 2010
Available online 23 June 2010

Keywords:
Implicit radiation hydrodynamics
Lagrangian meshes
Finite difference scheme
Point explosion problem
Self similar solutions
Asymptotic convergence analysis

ABSTRACT

A fully implicit finite difference scheme has been developed to solve the hydrodynamic equations coupled with radiation transport. Solution of the time-dependent radiation transport equation is obtained using the discrete ordinates method and the energy flow into the Lagrangian meshes as a result of radiation interaction is fully accounted for. A tri-diagonal matrix system is solved at each time step to determine the hydrodynamic variables implicitly. The results obtained from this fully implicit radiation hydrodynamics code in the planar geometry agrees well with the scaling law for radiation driven strong shock propagation in aluminium. For the point explosion problem the self similar solutions are compared with results for pure hydrodynamic case in spherical geometry. Results obtained when radiation interaction is also accounted agree with those of point explosion with heat conduction for lower input energies. Having, thus, benchmarked the code, self convergence of the method w.r.t. time step is studied in detail for both the planar and spherical problems. Spatial as well as temporal convergence rates are $\simeq 1$ as expected from the difference forms of mass, momentum and energy conservation equations. This shows that the asymptotic convergence rate of the code is realized properly.

1. Introduction

Radiation transport and its interaction with matter via emission, absorption and scattering of radiation have a substantial effect on both the state and the motion of materials in high temperature hydrodynamic flows occurring in inertial confinement fusion (ICF), strong explosions and astrophysical systems [1]. For many applications the dynamics can be considered non-relativistic since the flow velocities are much less than the speed of light. In order to describe properly the dynamics of the radiating flow, it is necessary to solve the full time-dependent radiation transport equation as very short time scales ($t_R \sim l/c$ or $t_\lambda \sim \lambda_p/c$ corresponding to a photon flight time over a characteristic structural length l, or over a photon mean free path λ_p) are to be considered [2]. Two methods commonly used are non-equilibrium diffusion theory [3,4] and radiation heat conduction approximation [1]. The former is valid for optically thick bodies, where the density gradients are small and the angular distribution of photons is nearly isotropic. The conduction approximation is applicable only for slower hydrodynamic time scales when matter and radiation are in local thermodynamic equilibrium so that the radiant energy flux is proportional to temperature gradient [1]. Use of Eddington's factor for closing the first two moment equations is yet another approach followed in radiation hydrodynamics [5]. Radiative phenomena occur on time scales that differ by many orders of magnitude from those characterizing hydrodynamic flow. This leads to significant computational challenges in the efficient modeling of radiation hydrodynamics.

In this paper we solve the equations of hydrodynamics and the time dependent radiation transport equation fully implicitly. The anisotropy in the angular distribution of photons is treated in a direct way using the discrete ordinates method.

* Corresponding author. Tel.: +91 22 25593959; fax: +91 22 25505151.
E-mail address: karabi.barc@gmail.com (K. Ghosh).

0021-9991/$ - see front matter © 2010 Elsevier Inc. All rights reserved.
doi:10.1016/j.jcp.2010.06.031

Finite difference analysis is used for the Lagrangian meshes to obtain the thermodynamic variables. The hydrodynamic evolution of the system is considered in a fully implicit manner by solving a tridiagonal system of equations to obtain the velocities. The pressures and temperatures are converged iteratively.

Earlier studies on the non-equilibrium radiation diffusion calculations show that the accuracy of the solution increases on converging the non-linearities within a time step and increasing benefit is obtained as the problem becomes more and more nonlinear and faster [6,7].

The organization of the paper is as follows: In Section 2 we discuss the finite difference scheme for solving the hydrodynamic equations followed by the solution procedure of the radiation transport equation and their coupling together to result in an implicit radiation hydrodynamics code. Section 3 presents the results obtained using this fully implicit one-dimensional radiation hydrodynamics code for the problems of shock propagation in aluminium and the point explosion problem including radiation hydrodynamics. These benchmark results, thus, prove the validity of the methods. Next, extensive results of asymptotic convergence studies for both temporal and spatial convergence are presented. Finally the conclusions of this paper are presented in Section 4.

2. Simulation model

2.1. Implicit finite difference scheme for solving the hydrodynamic equations using a Lagrangian grid

2.1.1. Grid structure

For hydrodynamic calculations, the medium is divided into a number of cells as shown in Fig. 1. The coordinate of the ith vertex is denoted by r_i and the region between the $(i-1)$ and ith vertices is the ith cell. The density of the ith grid is ρ_i and its mass is given by

$$m_i = \acute{c} \times \rho_i \times (r_i^{\delta} - r_{i-1}^{\delta}) \tag{1}$$

with $\acute{c} = 1, \pi, (4/3) \times \pi$ and $\delta = 1, 2, 3$ for planar, cylindrical and spherical geometries, respectively. Velocity of the ith vertex is denoted by u_i and P_i, V_i, $T_{ion,i}$, $T_{elec,i}$,$E_{ion,i}$ and $E_{elec,i}$ are the total pressure, specific volume, temperature and the specific internal energy of ions and electrons in the ith mesh, respectively.

2.1.2. Lagrangian step

During a time interval Δt the vertices r_i of the cells move as (with an error in position $O(\Delta t)^2$)

$$\tilde{r}_i = r_i + u_i^{\star} \Delta t, \tag{2}$$

$$u_i^{\star} = (1/2)(u_i + \tilde{u}_i), \tag{3}$$

where $u_i^{\star}$ is the average of velocity values at the beginning and end of the Lagrangian step, u_i and $\tilde{u}_i$, respectively.

2.1.3. Discretized form of the hydrodynamic equations

In the Lagrangian formulation of hydrodynamics, the mass of each cell remains constant thereby enforcing mass conservation.

The Lagrangian differential equation for the conservation of momentum is:

$$\rho \frac{d\vec{u}}{dt} = -\vec{\nabla} P. \tag{4}$$

Here, the total pressure is the sum of the electron and ion pressures i.e. $P = P_{ion} + P_{elec}$.

In this paper we neglect all terms $O(u/c)$ from the hydrodynamics as well as radiation transport equations. These equations are valid in the low radiation energy-density regime where radiation momentum deposition to the material is not important [8] and for radiative flows where the fluid speed u is much smaller than speed of light c [9]. In fact, for the problems analyzed here, (u/c) is in the range of $\sim$0.001 only. Our aim is to investigate the minimal numerical model for radiation hydrodynamics, where radiation is coupled only to electron energy equation via absorption and emission processes. Therefore, we do not consider radiation momentum terms arising from radiation transport in material momentum and energy equations.

Eq. (4) can be discretized, for the velocity $\tilde{u}_i$ at the end of the time step, in terms of the pressures $P_i^{1/2}$ and $P_{i+1}^{1/2}$ in the ith and $i+1$th meshes after half time step [10]:

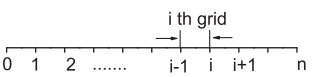

Fig. 1. Grid structure.

$$\tilde{u}_i = u_i - \frac{\left(P_{i+1}^{1/2} - P_i^{1/2}\right)\Delta t}{\rho_{i+1}\left(r_{i+1/2} - r_i\right) + \rho_i\left(r_i - r_{i-1/2}\right)}. \tag{5}$$

The velocity in the ith mesh $\tilde{u}_i$ is determined by the pressure in the ith and $i+1$th meshes and hence all the meshes are connected. Mass conservation equation can be used to eliminate the pressures at half time step to obtain an equation relating the present time step velocities in the adjacent meshes as follows:

The equation describing conservation of mass is

$$\frac{d\rho}{dt} = -\rho(\vec{\nabla}\cdot\vec{u}), \tag{6}$$

where ρ is the mass density of the medium. This equation can be rewritten in terms of pressure using the relation, $\frac{dP}{dt} = \left(\frac{dP}{d\rho}\right)_S \frac{d\rho}{dt} = v^2\frac{d\rho}{dt}$ where $v = \sqrt{\left(\frac{dP}{d\rho}\right)_S}$ is the adiabatic sound speed. Therefore, Eq. (6) becomes

$$\frac{dP}{dt} = -v^2\rho\vec{\nabla}\cdot\vec{u}. \tag{7}$$

This can be written for all the one dimensional co-ordinate systems as

$$\frac{dP}{dt} = -v^2\rho\frac{1}{r^\alpha}\frac{d}{dr}r^\alpha u, \tag{8}$$

where $\alpha = 0, 1, 2$ for planar, cylindrical and spherical geometries. This equation can be discretized to obtain the change in total pressure along a Lagrangian trajectory in terms of the velocity $\tilde{u}_i$ at the end of the time step [10]:

$$P_i^{1/2} = P_i + q_i - \rho_i v_i^2 \frac{1}{r_{i-1/2}^\alpha} \times \left[\frac{r_i^\alpha\tilde{u}_i - r_{i-1}^\alpha\tilde{u}_{i-1}}{r_i - r_{i-1}}\right]\frac{\Delta t}{2} \tag{9}$$

and

$$P_{i+1}^{1/2} = P_{i+1} + q_{i+1} - \rho_{i+1} v_{i+1}^2 \frac{1}{r_{i+1/2}^\alpha} \times \left[\frac{r_{i+1}^\alpha\tilde{u}_{i+1} - r_i^\alpha\tilde{u}_i}{r_{i+1} - r_i}\right]\frac{\Delta t}{2}. \tag{10}$$

Here, q_i is the quadratic Von Neumann and Richtmyer artificial viscosity in the ith mesh [11]:

$$q_i = \frac{\acute{k}(\rho_i\Delta x_i)^2}{V_i}\left(\frac{dV_i}{dt}\right)^2, \tag{11}$$

where $\acute{k}$ ($\simeq 3$) is a dimensionless constant.

Using Eqs. (9) and (10), $P_i^{1/2}$ and $P_{i+1}^{1/2}$ in Eq. (5) are eliminated to obtain a tridiagonal system of equations for $\tilde{u}_i$:

$$-A_i\tilde{u}_{i+1} + B_i\tilde{u}_i - C_i\tilde{u}_{i-1} = D_i, \tag{12}$$

where

$$A_i = \frac{\rho_{i+1}(v_{i+1}\Delta t)^2}{2(\rho\Delta r)_i} \times \frac{r_{i+1}^\alpha}{r_{i+1/2}^\alpha(r_{i+1} - r_i)}, \tag{14}$$

$$B_i = 1 + \frac{\rho_{i+1}(v_{i+1}\Delta t)^2}{2(\rho\Delta r)_i} \times \frac{r_i^\alpha}{r_{i+1/2}^\alpha(r_{i+1} - r_i)} + \frac{\rho_i(v_i\Delta t)^2}{2(\rho\Delta r)_i} \times \frac{r_i^\alpha}{r_{i-1/2}^\alpha(r_i - r_{i-1})}, \tag{15}$$

$$C_i = \frac{\rho_i(v_i\Delta t)^2}{2(\rho\Delta r)_i} \times \frac{r_{i-1}^\alpha}{r_{i-1/2}^\alpha(r_i - r_{i-1})}, \tag{16}$$

$$D_i = u_i - \frac{\Delta t}{(\rho\Delta r)_i}[P_{i+1} + q_{i+1} - P_i - q_i] \tag{17}$$

with

$$(\rho\Delta r)_i = \rho_{i+1}\left(r_{i+1/2} - r_i\right) + \rho_i\left(r_i - r_{i-1/2}\right). \tag{18}$$

The energy equations, for the ions and electrons, expressed in terms of temperature are

$$\rho\left[C_{Vion}\frac{\partial T_{ion}}{\partial t} + \frac{\partial E_{ion}}{\partial V}\frac{\partial V}{\partial t}\right] = -\frac{P_{ion}}{V}\frac{\partial V}{\partial t} - P_{ie} \tag{19}$$

and

$$\rho\left[C_{Velec}\frac{\partial T_{elec}}{\partial t}+\frac{\partial E_{elec}}{\partial V}\frac{\partial V}{\partial t}\right]=-\frac{P_{elec}}{V}\frac{\partial V}{\partial t}+\sigma_R(T_{elec})[E_R(r,T_{elec})-B(T_{elec})]+P_{ie}, \tag{20}$$

where E_{ion} and E_{elec} are the specific internal energies and V is specific volume. $\sigma_R(T_{elec})$ is the Rosseland opacity, $E_R(r,T_{elec})$ is the radiation energy flux and $\sigma_R(T_{elec})$ $B(T_{elec})$ is radiation emission rate. P_{ie} is the ion–electron energy exchange term given by

$$P_{ie}(Tergs/cm^3/\mu s)=2.704\times10^{-40}n_{elec}\ n_{ion}\times\frac{T_{ion}-T_{elec}}{T_{elec}^{1.5}}M^{-1}Z^2\times\ln\Lambda \tag{21}$$

with ion and electron temperatures expressed in keV. Further, 'n_{elec}' and 'n_{ion}' are the number densities of electrons and ions, M is the mass number and Z is the charge of the ions. Here the Coulomb logarithm for ion–electron collision is [12]

$$\ln\Lambda=\max\left\{1,\left(23-\ln[(n_{elec})^{0.5}ZT_{elec}^{-1.5}]\right)\right\} \tag{22}$$

with T_{elec} expressed in eV.

The discrete form of the energy equations for ions and electrons are

$$T_{ion,i}^{n,k}=T_{ion,i}^{n-1}-\left(P_{ion,i}^{n,k-1}\Delta V_i^{n,k}+\frac{P_{ie}^{n,k-1}\Delta t}{\rho_i^{n,k-1}}+\delta_{ion}^{n,k-1}\Delta V_i^{n,k}\right)\Big/C_{Vion,i}^{n,k-1} \tag{23}$$

and

$$T_{elec,i}^{n,k}=T_{elec,i}^{n,k-1}+\frac{\rho_i^{n,k-1}C_{Velec,i}^{n,k-1}\left(T_{elec,i}^{n-1}-T_{elec,i}^{n,k-1}\right)}{\Delta tD_i^{n,k-1}}+\left(\frac{\sigma_{Ri}^{n,k-1}}{D_i^{n,k-1}}\right)\left(E_i^{n,k}-B_i^{n,k-1}\right)-\frac{\left(P_{elec}^{n,k-1}+\delta_{elec}^{n,k-1}\right)\rho_i^{n,k-1}\Delta V_i^{n,k}}{\Delta tD_i^{n,k-1}}+P_{ie}^{n,k-1}/D_i^{n,k-1}, \tag{24}$$

where

$$D_i^{n,k-1}=\frac{\rho_i^{n,k}C_{Velec,i}^{n,k-1}}{\Delta t_n}+\sigma_{Ri}^{n,k-1}C_{v,Ri}^{n,k-1}, \tag{25}$$

$$\delta_{ion}^{n,k-1}=\left(\frac{\partial E_{ion}}{\partial V}\right)_i^{n,k-1}, \tag{26}$$

$$\delta_{elec}^{n,k-1}=\left(\frac{\partial E_{elec}}{\partial V}\right)_i^{n,k-1}, \tag{27}$$

$$C_{vRi}^{n,k-1}=4ac\left(T_{elec,i}^{n,k-1}\right)^3 \tag{28}$$

with 'n' and 'k' denoting the time step and iteration index, respectively. Also, the constants a (= $4\sigma/c$), $\sigma$and c denote the radiation constant, Stefan's constant and the speed of light, respectively. Stefan–Boltzmann law, $B(T_{elec})=acT_{elec}^4$, has been used explicitly in these equations.

2.2. Discrete ordinates method for solving the radiation transport equation

In the Gray approximation, or one group model, the time-dependent radiation transport equation in a stationary medium is

$$\frac{1}{c}\frac{\partial I}{\partial t}+\vec{\Omega}.\vec{\nabla}I+(\sigma_R(T)+\sigma_s)I(\vec{r},\vec{\Omega},t)=\frac{\sigma_R(T)B(T)}{4\pi}+\frac{\sigma_s}{4\pi}\int I(\vec{r},\vec{\Omega}',t)d\vec{\Omega}', \tag{29}$$

where $I(\vec{r},\vec{\Omega},t)$ is the radiation intensity, due to photons moving in the direction $\vec{\Omega}$, at space point $\vec{r}$ and time t. Here $\sigma_R(T)$ is the one group radiation opacity, which is assumed to be calculated by Rosseland weighing, at electron temperature T (the subscript of T_{elec} is dropped for convenience). As already mentioned, $B(T)$ is the radiation energy flux emitted by the medium which is given by the Stefan–Boltzmann law $B(T)=acT^4$. The radiation constant a is $\simeq$137 if T is in keV and c in cm/μs. This formula for the emission rate follows from the local thermodynamic equilibrium (LTE) approximation, which is assumed in the present model. The scattering cross-section σ_s, representing Thomson scattering is assumed to be isotropic and independent of temperature. In the Lagrangian framework the radiation transport equation for a planar medium is

$$\frac{1}{c}\rho\frac{\partial}{\partial t}\left(\frac{I}{\rho}\right)+\mu\frac{\partial I}{\partial x}+(\sigma_R(T)+\sigma_s)I(x,\mu,t)=\frac{\sigma_R(T)B(T)}{2}+\frac{\sigma_s}{2}\int_{-1}^{1}I(x,\mu\prime,t)\,d\mu', \tag{30}$$

where $I(x,\mu,t)$ is the radiation intensity along a direction at an angle $cos^{-1}(\mu)$ to the x-axis. The term $\rho\frac{\partial}{\partial t}\left(\frac{I}{\rho}\right)$ in this equation arises due to the Lagrange scheme used in solving the hydrodynamic equations.

Backward difference formula for the time derivative gives

$$\mu\frac{\partial I^{n,k}}{\partial x}+\left[\sigma_R^{n,k-1}+(c\Delta t)^{-1}+\sigma_s\right]I^{n,k}=\frac{\sigma_R^{n,k-1}B^{n,k-1}}{2}+\frac{\sigma_s}{2}\int_{-1}^{1}I^{n,k}(\mu\prime)d\mu\prime+\frac{\rho^{n,k-1}}{\rho^{n-1}}I^{n-1}(c\Delta t)^{-1}. \tag{31}$$

Here, 'n' and 'k' denote the time step and iteration index for temperature, respectively. This iteration arises because the opacity $\sigma_R(T)$ and the radiation emission rate $\sigma_R(T)B(T)$ are functions of the local temperature T. The converged spatial temperature distribution is assumed to be known for the hydrodynamic cycle for the previous time step. Starting with the corresponding values of $\sigma_R(T)$ and $B(T)$, denoted by $\sigma_R^{n,0}$ and $B^{n,0}$, the radiation energy fluxes are obtained from the solution of the transport equation Eq. (31). The method of solution, well known in neutron transport theory, is briefly discussed below. This is used in the electron energy equation of hydrodynamics (Eq. (24)) to obtain a new temperature distribution and corresponding values of $\sigma_R^{n,1}$ and $B^{n,1}$. The transport equation is again solved using these new estimates and the iterations are continued until the temperature distribution converges.

Finally the transport equation can be expressed in conservation form in spherical geometry as

$$\frac{\mu}{r^2}\frac{\partial}{\partial r}(r^2I^{n,k})+\frac{\partial}{\partial\mu}\left[\frac{(1-\mu^2)I^{n,k}}{r}\right]+\sigma I^{n,k}=Q(r,\mu) \tag{32}$$

with

$$\sigma=\sigma_R^{n,k-1}+(c\Delta t)^{-1}+\sigma_s, \tag{33}$$

$$Q(r,\mu)=\frac{\sigma_R^{n,k-1}B^{n,k-1}}{2}+\frac{\sigma_s}{2}\int_{-1}^{1}I^{n,k}(\mu\prime)d\mu\prime+\frac{\rho^{n,k-1}}{\rho^{n-1}}I^{n-1}(c\Delta t)^{-1}, \tag{34}$$

where, the second term in Eq. (32) accounts for angular redistribution of photons during free flight. This term arises as a result of the local coordinate system used to describe the direction of propagation of photons. If this term is omitted, Eq. (32) reduces to that for planar medium and therefore a common method of solution can be applied.

A slightly more accurate linearization [13] can be introduced in Eqs. (31) and (32) by replacing $B^{n,k-1}$ with $B^{n,k}$. Then, a first order Taylor expansion can be used for the approximation $B^{n,k}=B^{n,k-1}+(\partial B/\partial T)^{n,k-1}(T^{n,k}-T^{n,k-1})$ from which $(T^{n,k}-T^{n,k-1})$ can be eliminated using Eq. (24). The convergence of this modified method for treating the non-linearity of the Planck function may be better compared to the simple iteration method. However, for the problems considered in this paper we have successfully used the iteration method.

To solve Eq. (32), it is written in the discrete angle variable as [14]

$$\frac{\mu_m}{r^2}\frac{\partial}{\partial r}(r^2I_m)+\frac{2}{r\omega_m}(\alpha_{m+1/2}I_{m+1/2}-\alpha_{m-1/2}I_{m-1/2})+\sigma I_m=Q_m, \tag{35}$$

where the indices 'n' and 'k' on I have been suppressed. Here m refers to a particular value of μ in the angular range $[-1,1]$ which is divided into M directions. The parameter ω_m is the weight attached to this direction whose value has been fixed according to the Gauss quadrature and $\alpha_{m\pm1/2}$ are the angular difference coefficients. I_m and $I_{m\pm1/2}$ are the intensities at the centres and the edges of the angular cell, respectively. The angle integrated balance equation for photons is satisfied if the "α-coefficients" obey the condition

$$\Sigma_{m=1}^{M}[\alpha_{m+1/2}I_{m+1/2}-\alpha_{m-1/2}I_{m-1/2}]=0. \tag{36}$$

As photons traversing along $\mu=\pm1$ are not redistributed during the flight, the α-coefficients also obey the boundary conditions

$$\alpha_{1/2}=\alpha_{M+1/2}=0. \tag{37}$$

For a spatially uniform and isotropic angular flux, Eq. (35) yields the recursion relation

$$\alpha_{m+1/2}=\alpha_{m-1/2}-\omega_m\mu_m \tag{38}$$

as the intensity $I(r,\mu)$ is a constant in this case.

The finite difference version of Eq. (35) in space is derived by integrating over a cell of volume V_i bounded by surfaces $A_{i\pm1/2}$ where $V_i=4\pi\int_{r-1/2}^{r+1/2}r^2dr=\frac{4\pi}{3}\left(r_{i+1/2}^3-r_{i-1/2}^3\right)$ and $A_{i\pm1/2}=4\pi r_{i\pm1/2}^2$. The discrete form of the transport equation in space and angle is thus obtained as

$$\frac{\mu_m}{V_i}[A_{i+1/2}I_{m,i+1/2}-A_{i-1/2}I_{m,i-1/2}]+\frac{2(A_{i+1/2}-A_{i-1/2})}{\omega_mV_i}\times[\alpha_{m+1/2}I_{m+1/2,i}-\alpha_{m-1/2}I_{m-1/2,i}]+\sigma I_{m,i}=Q_{m,i}. \tag{39}$$

The cell average intensity and source are given by

$$I_{m,i}=\frac{1}{V_i}4\pi\int_{r_{i-1/2}}^{r_{i+1/2}}r^2I_m(r)\,dr \tag{40}$$

and

$$Q_{m,i} = \frac{1}{V_i} 4\pi \int_{r_{i-1/2}}^{r_{i+1/2}} r^2 Q_m(r)\, dr, \tag{41}$$

respectively, where '*i*' specifies the spatial mesh. As mentioned earlier, planar geometry equations are obtained if the terms involving $\alpha_{m\pm1/2}$ are omitted and the replacements $V_i = r_{i+1/2} - r_{i-1/2}$ and $A_{i+1/2} = 1$ are made. Thus, both geometries can be treated on the same lines using this approach. The difference scheme is completed by assuming that the intensity varies exponentially between the two adjacent faces of a cell both spatially and angularly so that the centered intensity $I_{m,i}$ can be expressed as [15]:

$$I_{m,i} = I_{m,i-1/2} \exp\left[-\frac{1}{2}(r_{i+1/2} - r_{i-1/2})\right], \tag{42}$$

$$I_{m,i} = I_{m,i+1/2} \exp\left[+\frac{1}{2}(r_{i+1/2} - r_{i-1/2})\right], \tag{43}$$

where the radii $r_{i+1/2}$ and $r_{i-1/2}$ are expressed in particle mean free paths. These relations show that

$$I_{m,i}^2 = I_{m,i-1/2} I_{m,i+1/2} \tag{44}$$

for the spatial direction. Similarly, for the angular direction one gets

$$I_{m,i}^2 = I_{m-1/2,i} I_{m+1/2,i}. \tag{45}$$

Use of these difference schemes guarantees positivity of all the angular fluxes if $Q_{m,i}$ are positive. The symmetry of the intensity at the centre of the sphere is enforced by the conditions

$$I_{M+1-m,1/2} = I_{m,1/2}, \quad m = 1, 2, \ldots, M/2. \tag{46}$$

Dividing the spatial range into L intervals, for a vacuum boundary at $r_{L+1/2}$, we have

$$I_{m,L+1/2} = 0, \quad m = 1, 2, \ldots, M/2 \tag{47}$$

i.e., at the rightmost boundary the intensities are zero for all directions pointing towards the medium. Alternately, boundary sources, if present, can also be specified.

An iterative method is used to solve the transport equation to treat the scattering term. The radiation densities at the centre of the meshes are taken from the previous time step, thereby providing the source explicitly. The intensities $I_{1/2,i}$ for all meshes do not occur in Eq. (39) as $\alpha_{1/2} = 0$. Then the intensities $I_{3/2,i}$ are eliminated from this equation using the upwind scheme $I_{3/2,i} = I_{1,i}$. Starting from the boundary condition, viz, Eqs. (47), (39) and (44) can be used to determine these two intensities for all the spatial meshes '*i*'. Thereafter together with Eq. (45), the intensities for all the negative values of μ_m can be solved for. At the centre, the reflecting boundary condition given by Eq. (46) provide the starting intensities for the outward sweeps through all the spatial and angular meshes with positive values of μ_m.

This completes one space-angle sweep providing new estimates of radiation energy flux (at the mesh centres) given by:

$$E_{Ri}^{n,k} = \sum_m \omega_m I_{m,i} \Big/ \sum_m \omega_m, \tag{48}$$

where the sum extends over all directions M. The mesh-angle sweeps are repeated until the scattering source distribution converges to a specified accuracy. The rate of radiation energy absorbed by unit mass of the material in the ith mesh is

$$\varepsilon_i = \sigma_{Ri}^{n,k-1} \left[E_{Ri}^{n,k} - B_i^{n,k-1}\right] \Big/ \rho_i^{n,k}, \tag{49}$$

which determines the coupling between radiation transport and hydrodynamics.

2.3. Implicit radiation hydrodynamics solution method

The sample volume is divided into '*L*' meshes of equal width. The initial position and velocity of all the vertices are defined according to the problem under consideration. Also the initial pressure, temperature and internal energy of all the meshes are entered as input.

For any time step, the temperature of the incident radiation is obtained by interpolating the data for the radiation temperature as a function of time (as in the case of shock propagation in aluminium sheet or an ICF pellet implosion in a hohlraum). All the thermodynamic parameters for this time step are initialized using their corresponding values in the previous time step. It is important to note that the velocity u_i in Eqs. (3) and (17) and position r_i in Eq. (2) are the old variables and remain constant unless the pressure and temperature iterations for this time step converge.

The temperature iterations begin by solving the radiation transport equation for all the meshes which gives the energy flowing from radiation to matter.

The 1D Lagrangian step is a leapfrog scheme where new radial velocities $\tilde{u}_i$ arise due to acceleration by pressure gradient evaluated at half time step. This leads to a time implicit algorithm. The first step in the pressure iteration starts by solving the tridiagonal system of equations for the velocity of all the vertices. The sound speed is obtained from the equation of state (EOS) of that material. The new velocities and positions of all the vertices are obtained which are used to calculate the new density and change in volume of all the meshes. The total pressure is obtained by adding the Von Neumann and Richtmeyer artificial viscosity to the ion and electron pressures and solving the energy equations which takes into account both the energy flow from radiation and the work done by (or on) the meshes due to expansion (or contraction). The energy equations for ions and electrons are solved using the corresponding material EOS which provides the pressure and the specific heat at constant volume of the material (both ions and electrons). The hydrodynamic variables like the position, density, internal energy and velocity of all the meshes are updated. The convergence criterion for the total pressure is checked and if the relative error is greater than a fixed error criterion, the iteration for pressure is continued, i.e., the code goes back to solve the tridiagonal equations to obtain the velocities, positions, energies and so on. When the pressure converges according to the error criterion, the convergence for the electron temperature is checked in a similar manner. The maximum value of the error in electron temperature for all the meshes is noted and if this value exceeds the value acceptable by the error criterion, the temperature iterations are continued, i.e., transport equation, tridiagonal system of equations for velocity, etc., are solved, until the error criterion is satisfied. Thus the method is fully implicit as the velocities of all the vertices are obtained by solving a set of simultaneous equations. Also, both the temperature and pressure are converged simultaneously using the iterative method. Once both the pressure and temperature distributions converge, the position of the shock front is obtained by noting the pressure change and the new time step is estimated as follows:

The time step Δt is chosen so as to satisfy the Courant condition which demands that it is less than the time for a sound signal with velocity v to traverse the grid spacing Δx, $\frac{v\Delta t}{\Delta x} < C$ where the reduction factor C is referred to as the Courant number. The stability analysis of Von Neumann introduces additional reduction in time step due to the material compressibility [16].

The order of the S_n approximation may take the values 2, 4, 6 and 8. All the results presented in this paper have been generated using S_n approximation of order 4.

The above procedure is repeated up to the time we are interested in following the evolution of the system. The solution method described above is clearly depicted in the flowchart given in Fig. 2. The time step index is denoted by 'nh' and 'dt' is the time step taken. The iteration indices for electron temperature and total pressure are expressed as 'npt' and 'npp', respectively. 'Error1' and 'Error2' are the fractional errors in pressure and temperature, respectively, whereas 'eta1' and 'eta2' are those acceptable by the error criterion.

3. Results

3.1. Investigation of the performance of the scheme using benchmark problems

3.1.1. Shock propagation in aluminium

In the indirect drive inertial confinement fusion, high power laser beams are focused on the inner walls of high Z cavities or hohlraums, converting the driver energy to X-rays which implode the capsule. If the X-ray from the hohlraum is allowed to fall on an aluminium foil over a hole in the cavity, the low Z material absorbs the radiation and ablates generating a shock wave. Using strong shock wave theory, the radiation temperature in the cavity T_R can be correlated to the shock velocity u_s. The scaling law derived for aluminium is $T_R = 0.0126 u_s^{0.63}$, where T_R is in units of eV and u_s is in units of cm/s for a temperature range of 100–250 eV [17].

For the purpose of simulation, an aluminium foil of thickness 0.6 mm and unit cross section is chosen. It is subdivided into 300 meshes each of width 2×10^{-4} cm. An initial guess value of 10^{-7} μs is used for the time step. The equilibrium density of Al is 2.71 gm/cc. In the discrete ordinates method four angles are chosen. As the temperature attained for this test problem is somewhat low, the total energy equation is solved assuming that electrons and ions are at the same temperature (the material temperature). The EOS and Rosseland opacity for aluminium are given by

$$e = \frac{PV}{\gamma - 1} = \epsilon T^{\mu} V^{\nu}, \tag{50}$$

$$\kappa_R = l^{-1} T^{-\mu_R} V^{-\nu_R}. \tag{51}$$

Here $V = 1/\rho$ is the specific volume and $\gamma = 1 + \nu/(\mu - 1)$ is the adiabatic index. These power law functions, of temperature and density, where $\epsilon = 12.5$ in units of $10^{14} g^{\nu}\,\mathrm{cm}^{2-3\nu}\,\mathrm{s}^{-2}\,\mathrm{keV}^{-\mu}$, $l = 5$ in units of $g^{\nu_R}\,\mathrm{cm}^{1-\nu_R}\,\mathrm{keV}^{-\mu_R}$, $\mu = 1.145, \nu = 0.063, \mu_R = 3.8$ and $\nu_R = 1.5$ are the fitting parameters, are quite accurate in the temperature range of interest [18].

Using the fully implicit radiation hydrodynamics code, a number of simulations are carried out for different values of time independent incident radiation fluxes or temperatures. Corresponding shock velocities are then determined after the decay of initial transients. In Fig. 3. we show the comparison between the numerically obtained shock velocities for different radiation temperatures (points) and the scaling law for aluminium (line) mentioned earlier. Good agreement is observed in the temperature range where the scaling law is valid.

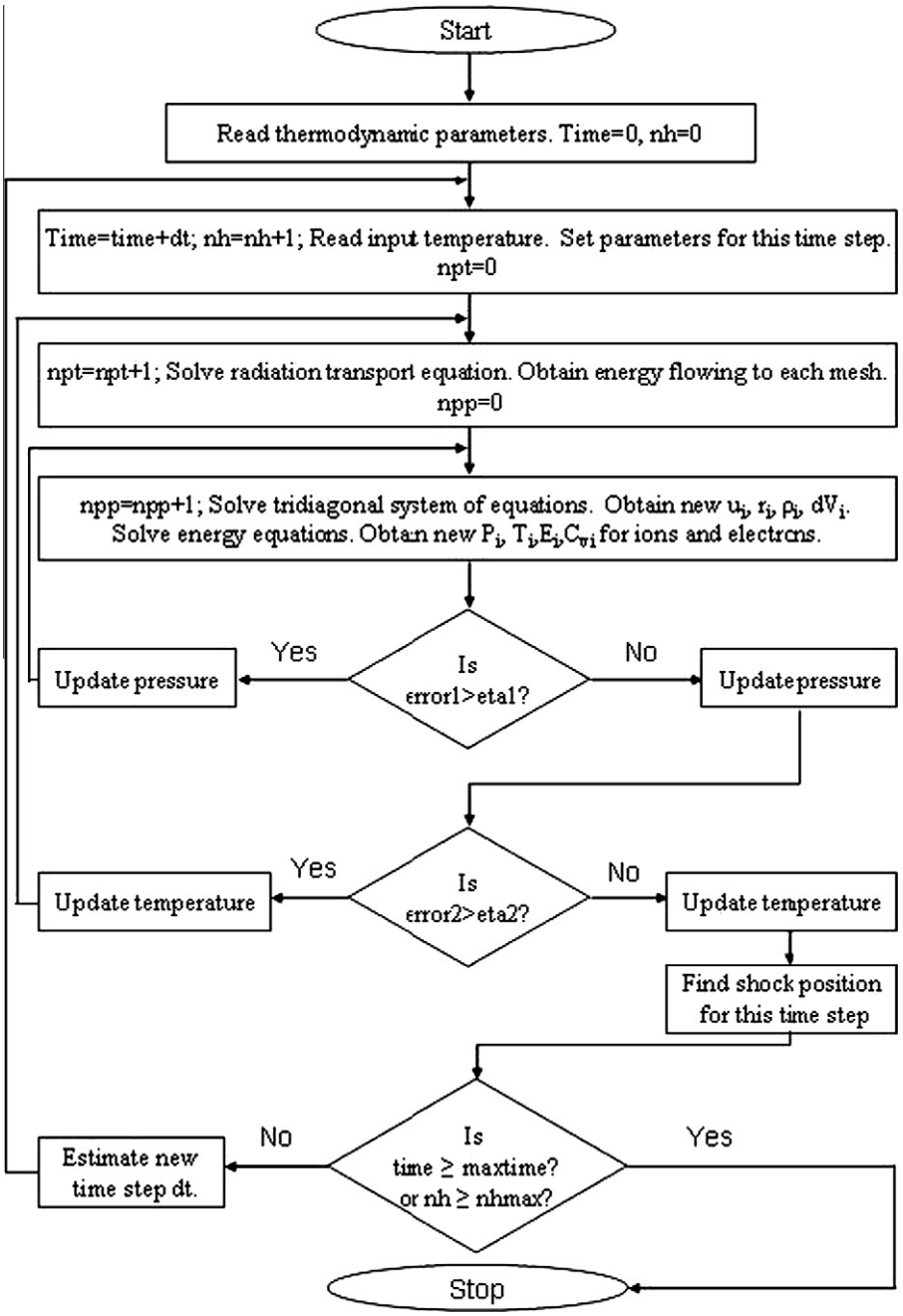

Fig. 2. Flowchart for the implicit 1D Radiation Hydrodynamics. Here, 'nh' is the time step index and 'dt' is the time step taken. The iteration indices for electron temperature and total pressure are 'npt' and 'npp', respectively. 'Error1' and 'Error2' are the fractional errors in pressure and temperature, respectively, whereas 'eta1' and 'eta2' are those acceptable by the error criterion.

Fig. 4 shows the various thermodynamic variables like velocity, pressure, density and material temperature after 2.5 ns when the radiation profile shown in Fig. 5 is incident on the outermost mesh. This radiation temperature profile is chosen so as to achieve nearly isentropic compression of the fuel pellet. The pulse is shaped in such a way that the pressure on the target surface gradually increases, so that the generated shock rises in strength. From Fig. 4 we observe that the outer meshes have ablated outwards while a shock wave has propagated inwards. At 2.5 ns, the shock is observed at 0.5 mm showing a peak in pressure and density. As the outer region has ablated, they move outwards with high velocities. The outermost mesh has moved to 1.2 mm. The meshes at the shock front move inwards showing negative velocities. Also the temperature profile shows that the region behind the the shock gets heated to about 160 eV. In Fig. 6 we plot the distance traversed by the shock

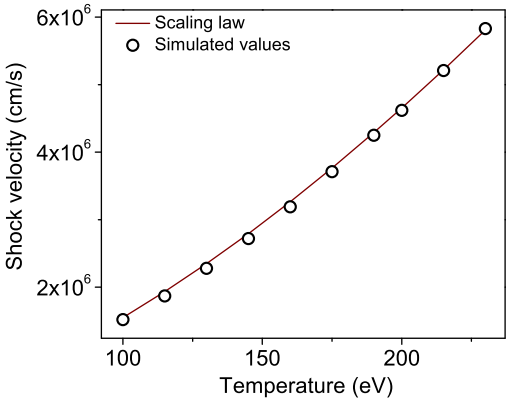

Fig. 3. Comparison of simulation data (points) with scaling law (line) relating shock velocity with the radiation temperature for aluminium.

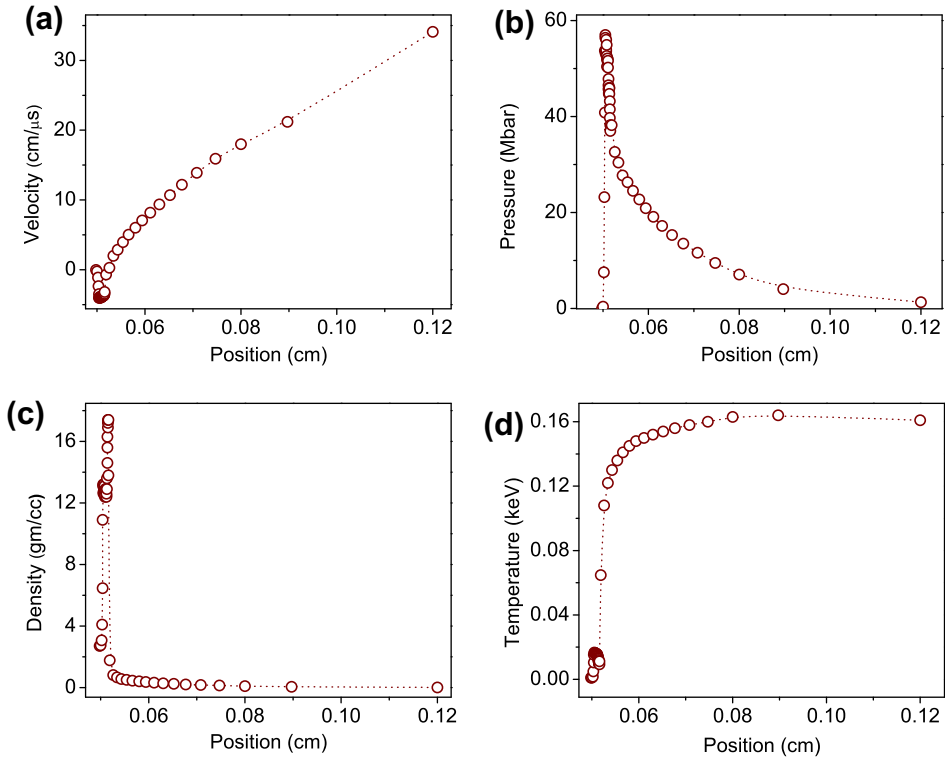

Fig. 4. Profiles of the thermodynamic variables: (a) velocity, (b) pressure, (c) density and (d) temperature in the region behind the shock as a function of position at $t = 2.5$ ns. The region ahead of the shock is undisturbed and retain initial values of the variables. The incident radiation temperature on the Al foil is shown in Fig. 5.

front as a function of time for the above radiation temperature profile. The shock velocity changes from 3.54 to 5.46 cm/μs at 1.5 ns when the incident radiation temperature increases to 200 eV.

All the runs in this study were done on a Pentium (4) computer having 1 GB of RAM operating at 3.4 GHz.

3.1.2. Point explosion problem

3.1.2.1. Sedov's self similar point explosion problem. The self similar problem of a strong point explosion was formulated and solved by Sedov [19]. The problem considers a perfect gas with constant specific heats and density ρ_0 in which a large amount of energy E is liberated at a point instantaneously. The shock wave propagates through the gas starting from the point where the energy is released. For numerical simulation, the energy E is assumed to be liberated in the first two meshes. The process is considered at a larger time t when the radius of the shock front $R(t) \gg r_0$, the radius of the region in which

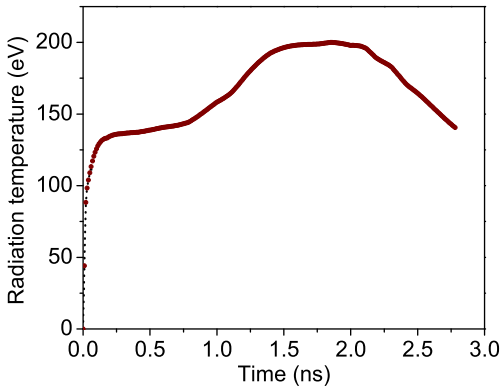

Fig. 5. Radiation temperature profile in the hohlraum for strong shock propagation in aluminium.

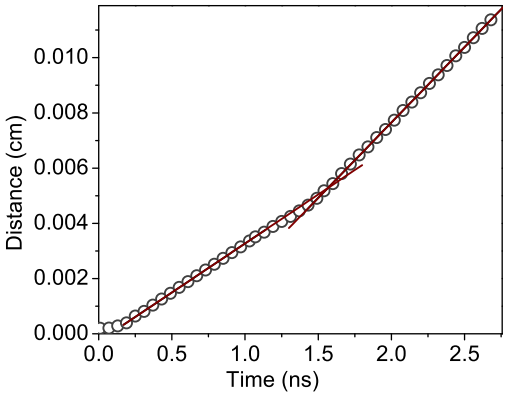

Fig. 6. Distance traversed by the shock front vs. time in Al foil for incident radiation temperature shown in Fig. 5. The two slopes correspond to the two plateaus in the radiation profile.

energy is released. It is also assumed that the process is sufficiently early so that the shock wave has not moved too far from the source. This ascertains that the shock strength is sufficiently large and it is possible to neglect the initial gas pressure P_0 or counter pressure in comparison with the pressure behind the shock wave [1].

Under the above assumptions, the gas motion is determined by four independent variables, viz, amount of energy released E, initial uniform density ρ_0, distance from the centre of the explosion r and time t. The dimensionless quantity $\xi = r/R$ serves as the similarity variable. The motion of the wavefront $R(t)$ is governed by the relationship

$$R = \xi_0 \left(\frac{E}{\rho_0}\right)^{1/5} t^{2/5}, \tag{52}$$

where ξ_0 is an independent variable. The propagation velocity of the shock wave is

$$D = \frac{2}{5}\xi_0^{5/2}\left(\frac{E}{\rho_0}\right)^{1/2} R^{-3/2}. \tag{53}$$

The parameters behind the shock front using the limiting formulas for a strong shock wave are

$$u_1 = \frac{2}{\gamma+1} D, \tag{54}$$

$$P_1 = \frac{2}{\gamma+1}\rho_0 D^2, \tag{55}$$

$$\rho_1 = \rho_0 \frac{\gamma+1}{\gamma-1}, \tag{56}$$

$$T_1 = \frac{P_1}{(\gamma-1)\rho_1 C_V}, \tag{57}$$

where C_V is the specific heat at constant volume and $\gamma = C_P/C_V$ is the ratio of specific heats. The distributions of velocity, pressure and density w.r.t. the radius are determined as functions of the dimensionless variable $\xi = r/R$. Since the motion is self-similar, the solution can be expressed in the form

$$u = u_1(t)\tilde{u}(\xi), \quad P = P_1(t)\tilde{P}(\xi), \quad \rho = \rho_1\tilde{\rho}(\xi), \tag{58}$$

where $\tilde{u}, \tilde{P}$ and $\tilde{\rho}$ are new dimensionless functions. The hydrodynamic equations, which are a system of three PDE's, are transformed into a system of three ordinary first-order differential equations for the three unknown functions $\tilde{u}, \tilde{P}$ and $\tilde{\rho}$ by substituting the expressions given by Eq. (58) into the hydrodynamic equations for the spherically symmetric case and transforming from r and t to ξ. The boundary condition satisfied by the solution at the shock front ($r = R$ or $\xi = 1$) is $\tilde{u} = \tilde{P} = \tilde{\rho} = 1$. The dimensionless parameter ξ_0, which depends on the specific heat ratio γ is obtained from the condition of conservation of energy evaluated with the solution obtained.

Also, the distributions of velocity, pressure, density and temperature behind the shock front are generated numerically using the hydrodynamics code without taking radiation interaction into account. Ideal D-T gas of density $\rho_0 = 1$ gm/cc and $\gamma = 1.4$ is filled inside a sphere of 1 cm radius with the region divided into 100 radial meshes each of width 0.01 cm. The initial internal energy per unit mass is chosen as 10^5 Tergs/gm for the first two meshes and zero for all the other meshes. An initial time step of 10^{-6} μs is chosen and the thermodynamic variables are obtained after a time 0.2 μs. As in the case of the problem of shock propagation in aluminium, the total energy equation is solved assuming that electrons and ions are at the same temperature (the material temperature). In Fig. 7 we compare the distribution of the functions P/P_1, u/u_1, ρ/ρ_1 and T/T_1 with respect to r/R obtained exactly by solving the ODEs as explained above (solid lines) with the results generated from our code (points). Good agreement between the numerical and theoretical results is observed. As is characteristic of a strong explosion, the gas density decreases extremely rapidly as we move away from the shock front as seen from Fig. 7. In the vicinity of the front the pressure decreases as we move towards the centre by a factor of 2–3 and then remains constant whereas the velocity curve rapidly becomes a straight line passing through the origin. The temperatures are very high at the centre and decreases smoothly at the shock front. As the particles at the centre are heated by a strong shock, they have very high entropy and hence high temperatures.

3.1.2.2. Point explosion problem with heat conduction. P. Reinicke and J. Meyer-ter-Vehn (RMV) analyzed the problem of point explosion with nonlinear heat conduction for an ideal gas equation of state and a heat conductivity depending on temperature and density in a power law form [20]. The problem combines the hydrodynamic (Sedov) point explosion with the spherically expanding nonlinear thermal wave. The RMV problem is a good test to determine the accuracy of coupling two distinct physics processes: hydrodynamics and radiation diffusion. Later on, Shestakov presented the results of point explosion with heat conduction using a coupled hydrodynamic diffusion code [21]. In this paper, we generate the results for the point explosion including radiation interaction using our fully implicit radiation hydrodynamics code. In the heat conduction approximation, the energy equation is written as

$$\frac{\partial}{\partial t}(\rho E) + \vec{\nabla}\cdot(\vec{u}(\rho E + P)) = -\vec{\nabla}.\vec{H}, \tag{59}$$

where the heat flux $H = -\chi\vec{\nabla}T$ and the conductivity is of the form $\chi = \chi_0\rho^{a_0}T^{b_0}$ where χ_0, a_0 and b_0 are constants. The conductivity can be related to Rosseland opacity as follows: $H = -\frac{c}{3\sigma_R}\vec{\nabla}E_R$ in the heat conduction approximation. Now, $E_R = aT^4$ and therefore, $H = -\frac{4acT^3}{3\sigma_R}\vec{\nabla}T$, so that $\chi = \frac{4acT^3}{3\sigma_R}$. The Rosseland opacity is assumed to vary with density and temperature as $\sigma_R = \sigma_0\rho^m T^{-n}$. Substituting the functional dependencies of conductivity and Rosseland opacity into the equation relating the two, we obtain $a_0 = -m$ and $b_0 = n + 3$. For the problem under consideration, $a_0 = -2$ and $b_0 = 6.5$. So, the Rosseland opac-

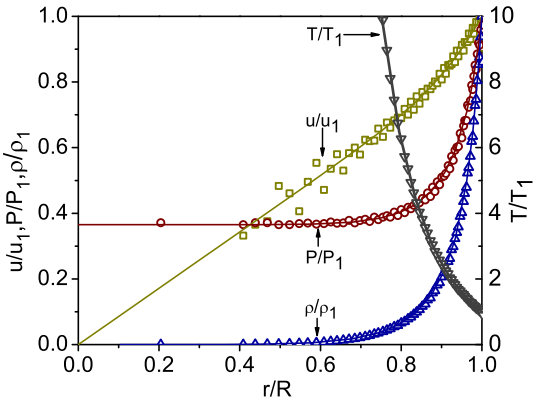

Fig. 7. Comparison of the scaled variables obtained from the simulation data in the pure hydrodynamic case (points) with the self similar solutions (lines) for the point explosion problem. Specific internal energy $E = 10^5$ Tergs/gm is deposited in the first two meshes and $\gamma = 1.4$.

ity used in our code is $\sigma_R = \sigma_0 \rho^2 T^{-3.5}$ with $\sigma_0 = \frac{4ac}{3\chi_0}$. As in the RMV problem, the initial gas density is assumed to be $\rho = g_0 r^k$ with $k = -(6b_0 - 1)/(2b_0 - 2a_0 + 1) = -2.111$ in this case. The thermodynamic variables are related by the ideal gas equation of state, $\frac{p}{\rho} = NkT = RT = (\gamma - 1)e = \Gamma T$. If energy is in unit of 10^{16} ergs, pressure in 10^{16} ergs/cc, temperature in keV and density in gm/cc, then we can set $\Gamma = g_0 = \chi_0 = 1$.

The normalized density, pressure, velocity and temperature obtained from our radiation hydrodynamic code for $\gamma = 5/4$ at 4.879 ns for a total energy of 16.9×10^{16} ergs deposited in the first mesh are shown in Fig. 8. The results agree with those published by RMV and those generated by Shestakov. The kink in ρ/ρ_1 and a sharp drop in T/T_1 at a distance of 0.57 cm are observed which shows that the heat front lags behind the shock front in this case. The smooth variation of temperature near the origin shows the effectiveness of radiative energy transfer from regions of high temperature. But for the unperturbed power law density profile ahead of the shock front, profiles of other variables are somewhat similar to point explosion problem without heat conduction.

For energy deposition of 235×10^{16} ergs, the heat front is found to move ahead of the shock front at 0.5145 ns in RMV problem. The perturbations in other variables (pressure and velocity) generated by the advancing heat front are observed by Shestakov also. However, the results of our radiation hydrodynamic code does not show these features. As shown in Fig. 9, the heat wave does not move beyond the shock wave and consequently all the variables are unperturbed ahead of the shock front. The reason behind this difference is the use of heat conduction approximation by RMV and Shestakov. For the well known Marshak wave propagation problem [22,23], it is found that diffusion approximations lead to a deeper penetration of radiation into the medium. However, this does not happen when full radiation transport is taken into account. Further, in the heat conduction approximation, radiation energy density does not evolve independently to reach a distribution in equilibrium with material temperature. The heat flux $H = -\frac{4ac}{3\sigma_0}\rho^{-2}T^{6.5}\vec{\nabla}T$, because of its temperature dependence, peaks beyond the region where $|\vec{\nabla}T|$ begins to decrease. For very high energy deposition, the heat front apparently moves ahead of the shock front due to pre-heating by radiation conduction. We are attempting a quantitative characterization of this phenomenon.

3.2. Asymptotic convergence analysis of the code

Asymptotic convergence analysis is performed for conducting verification analysis of the code. The asymptotic convergence rate quantifies the convergence properties of the software implementation (code) of a numerical algorithm for solving the discretized forms of continuum equations [24].

In the Lagrangian formalism as used in our code though the mesh sizes vary non uniformly with time, the mass of a mesh remains constant. For any variable ξcomputed for a given mesh of mass Δm_i and uniform time step Δt_l, the fundamental *ansatz* of pointwise convergence analysis is that the difference between the exact and the computed solutions can be expanded as a function of the mass and temporal zone sizes:

$$\xi^* - \xi_i^l = \epsilon_0 + A(\Delta m_i)^p + B(\Delta t_l)^q + C(\Delta m_i)^r(\Delta t_l)^s + O((\Delta m_i)^p, (\Delta t_l)^q, (\Delta m_i)^r(\Delta t_l)^s), \tag{60}$$

where ξ^* is the exact value, ξ_i^l is the value computed on the grid of zone mass Δm_i and time step Δt_l, ϵ_0 is the zeroth order error, A is the spatial/mass-wise convergence coefficient, p is the mass-wise convergence rate, B is the temporal convergence coefficient, q is the temporal convergence rate, C is the spatio- temporal convergence coefficient and $r + s$ is the spatio-temporal convergence rate.

Our code verification for both planar and spherical cases consider the global mass-wise and temporal convergence separately.

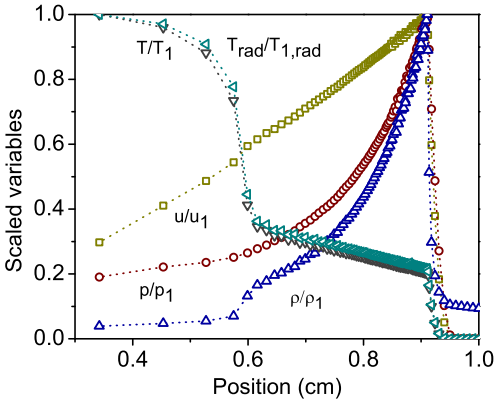

Fig. 8. Profiles of the scaled thermodynamic variables at $t = 4.879$ ns for the point explosion problem including radiation interaction for $\gamma = 5/4$. Total energy 16.9×10^{16} ergs is deposited at $t = 0$ in the first mesh.

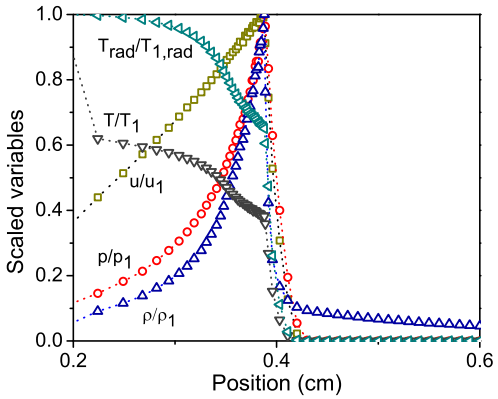

Fig. 9. Profiles of the scaled thermodynamic variables at $t = 0.5145$ ns for the point explosion problem including radiation interaction for $\gamma = 5/4$. Total energy 235×10^{16} ergs is deposited at $t = 0$ in the first mesh.

3.2.1. Global mass-wise convergence analysis

We employ the *ansatz* that the norm of the difference between the exact and computed solutions for the same time step Δt is

$$\|\xi^* - \xi_c\| = A(\Delta m)^p. \tag{61}$$

Since the exact solution ξ^* is unknown for the radiation hydrodynamics problem, we replace ξ^* by ξ_f where ξ_f is the value obtained for a very fine mesh ($\Delta m_f = \Delta m/\sigma^3$ and $\Delta m = \rho \Delta r$). The values ξ_m and ξ_i are also obtained for $\Delta m_m = \Delta m/\sigma$ and $\Delta m_i = \Delta m/\sigma^2$, respectively. Hence the mass-wise convergence rate p is obtained from the following errors:

$$\|\xi_f - \xi_c\| = A(\Delta m)^p, \tag{62}$$
$$\|\xi_f - \xi_m\| = A(\Delta m/\sigma)^p, \tag{63}$$
$$\|\xi_f - \xi_i\| = A(\Delta m/\sigma^2)^p. \tag{64}$$

Applying logarithm to both sides and plotting the logarithm of the norm of the errors as a function of the logarithm of the mesh width, the slope of the line gives the mass-wise convergence rate p.

$$log\|\xi_f - \xi_c\| = logA + p\ log(\Delta m), \tag{65}$$
$$log\|\xi_f - \xi_m\| = logA + p\ log(\Delta m/\sigma), \tag{66}$$
$$log\|\xi_f - \xi_i\| = logA + p\ log(\Delta m/\sigma^2). \tag{67}$$

For N number of meshes, the L_1 norm is defined as

$$\|\xi_2 - \xi_1\|_1 = \Delta m \Sigma_{i=1}^{N} |\xi_2 - \xi_1|$$

and L_2 norm as

$$\|\xi_2 - \xi_1\|_2 = \sqrt{\Delta m \Sigma_{i=1}^{N} |\xi_2 - \xi_1|^2}.$$

3.2.2. Global temporal convergence analysis

Similar to the mass-wise convergence analysis, the *ansatz* employed is that the norm of the difference between the exact and computed solutions for the same mass of the mesh Δm is

$\|\xi^* - \xi_c\| = \epsilon_m + B(\Delta t)^q$ where ϵ_m is the mass-wise error which dominates over the temporal error and hence needs to be accounted. However, the exact solution ξ^* being unknown, ξ^* is replaced by ξ_f where ξ_f is the value obtained for a very small time step ($\Delta t_f = \Delta t/\tau^3$). The values ξ_m and ξ_i are similarly obtained for $\Delta t_m = \Delta t/\tau$ and $\Delta\, t_i = \Delta t/\tau^2$, respectively. Replacing ξ^* by ξ_f, ϵ_m on the R.H.S. gets cancelled as all the variables ξ_f, ξ_i, ξ_m, ξ_c, etc., are obtained for the same value of mass of a mesh. Thus the temporal convergence rate q is obtained from the following equations:

$$log\|\xi_f - \xi_c\| = logB + q\ log(\Delta t), \tag{68}$$
$$log\|\xi_f - \xi_m\| = logB + q\ log(\Delta t/\tau), \tag{69}$$
$$log\|\xi_f - \xi_i\| = logB + q\ log(\Delta t/\tau^2). \tag{70}$$

A plot of the logarithm of the L_1 and L_2 norms of the errors in total internal energy for both spatial/mass-wise and temporal convergence are shown in Fig. 10 for the problem of shock propagation in aluminium foil. In all the cases the convergence

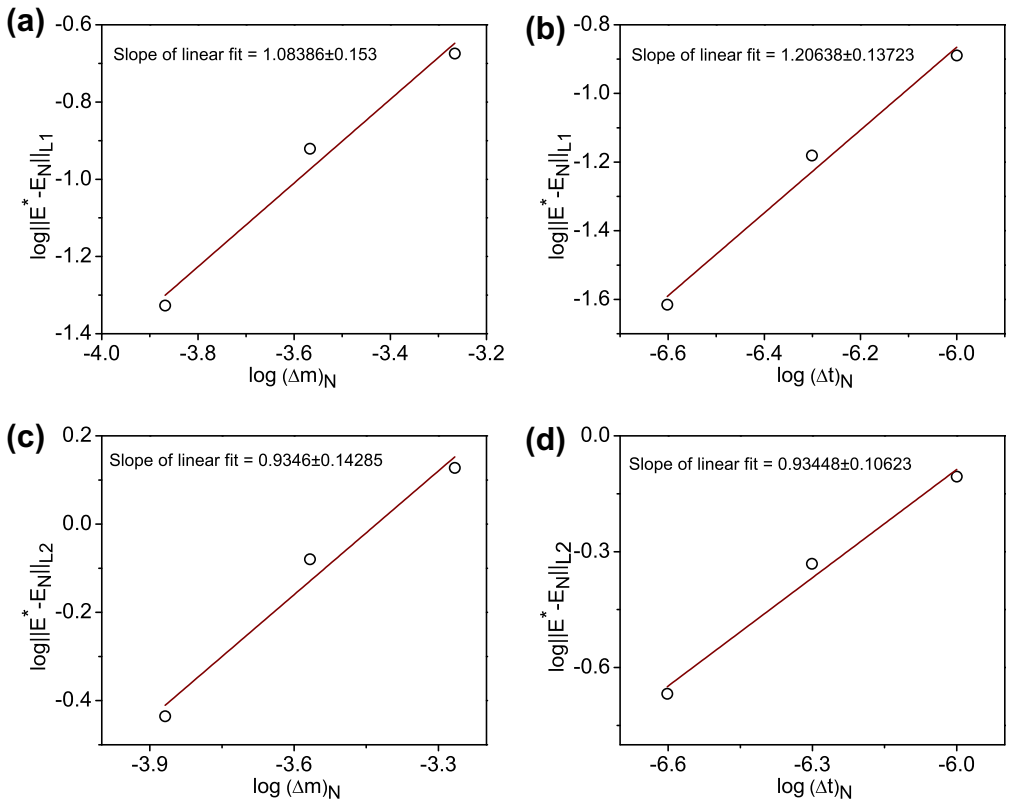

Fig. 10. (a) Spatial convergence rate for the L_1 norm. (b) Temporal convergence rate for the L_1 norm. (c) Spatial convergence rate for the L_2 norm and (d) temporal convergence rate for the L_2 norm obtained for the error in the thermodynamic variable internal energy (E) for the problem of shock propagation in Al foil.

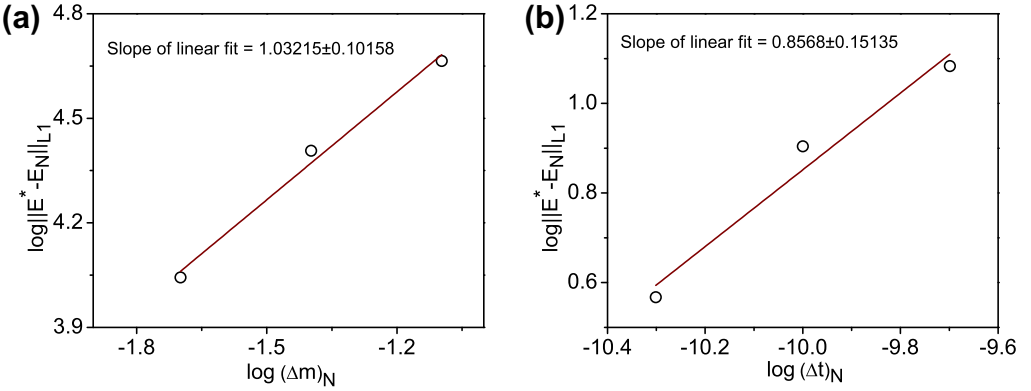

Fig. 11. (a) Spatial and (b) Temporal convergence rate for the L_1 norm obtained for the error in the thermodynamic variable internal energy (E) for the problem of point explosion with radiation interaction (total energy 235×10^{16} ergs is deposited).

rates are $\simeq 1$ as expected from the discretization of the mass, momentum and energy conservation equations (as explained in Appendix A). Similar convergence rates ($\simeq 1$) are observed for the other thermodynamic variables like velocity, pressure, density and temperature. Similarly, for the spherical case of point explosion problem with radiation transport, the spatial and temporal convergence rates are $\simeq 1$ for the L_1 norm as depicted for the total internal energy in Fig. 11.

4. Conclusions

In this paper we have developed and studied the performance of fully implicit radiation hydrodynamics scheme. The time-dependent radiation transport equation is solved and energy transfer to the medium is accounted exactly without invoking approximation methods. To validate the code, the results have been verified using the problem of shock propaga-

tion in aluminium foil in the planar geometry and the point explosion problem with heat conduction in the spherical geometry. The simulation results show good agreement with the theoretical solutions. For the purpose of verification, asymptotic convergence analysis is applied to both the problems of shock propagation in aluminium and the point explosion problem including full radiation transport. The temporal and mass-wise convergence rates are found to be $\simeq 1$ in agreement with the fact that the thermodynamic variables velocity, pressure, density, temperature and internal energy have an error $O(\Delta m)$ for constant time steps and $O(\Delta t)$ for a fixed mesh width on discretizing the respective conservation equations.

Acknowledgments

We thank one of the reviewers for important comments on consistent non-relativistic and low radiation energy-density approximations in radiation hydrodynamics.

Appendix A. Error arising from the discretization of mass, momentum and energy conservation equations

The position of a mesh at time t i.e., $\tilde{r}_i$ can be written in terms of the position at the previous time r_i by Taylor series expansion as

$$\tilde{r}_i = r_i + u_i \Delta t + \frac{a_i (\Delta t)^2}{2} + O(\Delta t)^3. \tag{A.1}$$

In the radiation hydrodynamics code, terms $O(\Delta t)^2$ has been neglected in writing Eq. (2). So, the error in position is $O(\Delta t)^2$. Also, $u = \frac{dr}{dt}$ and hence the error in velocity is $O(\Delta t)$.

Similarly, in writing Eqs. (9) and (10), i.e. the equation for conservation of mass in discrete form, since the gradient of velocity is written as a forward difference formula, the error in pressure is $O(\Delta t)$ for a constant mesh width i.e., the temporal convergence rate $\simeq 1$ and $O(\Delta m)$ for a constant time step, i.e., the spatial/mass-wise convergence rate $\simeq 1$. From the discrete form of the energy equations, i.e., Eq. (23), etc., it is observed that the temporal error in internal energy is $O(\Delta\, t)$ and mass-wise error is $O(\Delta m)$.

References

[1] Y.B. Zeldovich, Y.P. Raizer, Physics of Shock Waves and High-Temperature Hydrodynamic Phenomena, vols. I and II, Academic Press, New York, 1966.
[2] D. Mihalas, B.W. Mihalas, Foundations of Radiation Hydrodynamics, Oxford Univ. Press, New York, 1984.
[3] W. Dai, P.R. Woodward, Numerical simulation for radiation hydrodynamics. I. Diffusion limit, J. Comput. Phys. 142 (1998) 182.
[4] J.W. Bates et al, On consistent time-integration methods for radiation hydrodynamics in the equilibrium diffusion limit: low-energy-density regime, J. Comput. Phys. 167 (2001) 99.
[5] W. Dai, P.R. Woodward, Numerical simulation for radiation hydrodynamics. II. Transport limit, J. Comput. Phys. 157 (2000) 199.
[6] D.A. Knoll, W.J. Rider, G.L. Olson, Nonlinear convergence, accuracy, and time step control in nonequilibrium radiation diffusion, J. Quant. Spectrosc. Radiative Transf. 70 (2001) 25.
[7] C.C. Ober, J.N. Shadid, Studies on the accuracy of time-integration methods for the radiation–diffusion equations, J. Comput. Phys. 195 (2004) 743.
[8] R.B. Lowrie, D. Mihalas, J.E. Morel, Comoving-frame radiation transport for nonrelativistic fluid velocities, J. Quant. Spectrosc. Radiative Transfer 69 (2001) 291.
[9] R. Paul Drake, High-Energy-Density Physics, Fundamentals, Inertial Fusion and Experimental Astrophysics, Springer-Verlag, Berlin, Heidelberg, 2006. ISBN:10 3-540-29314-0 (Chapter 7).
[10] D. de Niem, E. Kuhrt, U. Motschmann, A volume-of-fluid method for simulation of compressible axisymmetric multi-material flow, Comput. Phys. Commun. 176 (2007) 170.
[11] J. Von Neumann, R.D. Richtmyer, A method for the numerical calculation of hydrodynamic shocks, J. Appl. Phys. 21 (1950) 232.
[12] J.D. Huba, NRL Plasma Formulary, vol. 35, Naval Research Lab, Washington, 2006.
[13] E. Larsen, A grey transport acceleration method for time-dependent radiative transfer problems, J. Comput. Phys. 78 (1988) 459.
[14] E.E. Lewis, W.F. Miller Jr., Computational Methods of Neutron Transport, John Wiley and Sons, New York, 1984.
[15] P. Barbucci, F. Di Pasquantonio, Exponential supplementary equations for S_N methods: the one-dimensional case, Nucl. Sci. Eng. 63 (1977) 179.
[16] M.L. Wilkins, Computer Simulation of Dynamic Phenomena, Springer-Verlag, Berlin, Heidelberg, New York, 1999, ISBN 3-540-63070-8.
[17] R.L. Kauffman et al, High temperatures in inertial confinement fusion radiation cavities heated with 0.35 μm light, Phys. Rev. Lett. 73 (1994) 2320.
[18] M. Basko, An improved version of the view factor method for simulating inertial confinement fusion hohlraums, Phys. Plasmas 3 (1996) 4148.
[19] L.I. Sedov, in: M. Holt (Ed.), Similarity and Dimensional Methods in Mechanics, fourth ed., Academic Press, New York, 1959. Gostekhizdat, Moscow, 1957, English transl..
[20] P. Reinicke, J. Meyer-ter-Vehn, The point explosion with heat conduction, Phys. Fluids A 3 (1991) 1807.
[21] A.I. Shestakov, Time-dependent simulations of point explosions with heat conduction, Phys. Fluids 11 (1999) 1091.
[22] B. Su, G.L. Olson, Non-grey benchmark results for two temperature non-equilibrium radiative transfer, J. Quant. Spectrosc. Radiative Transf. 62 (1999) 279.
[23] G.L. Olson, L.H. Auer, M.L. Hall, Diffusion, P_1, and other approximate forms of radiation transport, J. Quant. Spectrosc. Radiative Transf. 64 (2000) 619s.
[24] J.R. Kamm, W.J. Rider, J.S. Brock, Consistent Metrics for Code Verification, Los Alamos National Laboratory, LA-UR-02-3794, 2004.